Chemical Science

ROYAL SOCIETY OF CHEMISTRY

EDGE ARTICLE

View Article Online
View Journal

Cite this: DOI: 10.1039/d6sc02304e

All publication charges for this article have been paid for by the Royal Society of Chemistry

Liquid-crystal-assisted chiral nanoscintillator architectures with circular polarization degree exceeding 0.7 in X-ray radioluminescence

Ziyi Yuan,† Zejian Li,† Zitong Ling, Ke Wang and Chenlu He *

X-ray imaging stands as a fundamental technology in clinical diagnostics and industrial inspection, capitalizing on its exceptional material penetration capabilities. Conventional systems use achiral scintillators that produce unpolarized radioluminescence, limiting imaging to static, intensity-based detection. Herein, we report a dynamic X-ray imaging approach using chiral nanoscintillator architectures that generate circularly polarized radioluminescence (CPRL). By integrating perovskite nanocrystals with spectrum-matched cholesteric liquid crystals, we achieve a circular polarization degree of 0.75 in radioluminescence, along with X-ray imaging performance featuring a detection limit of 204 nGy s^{-1} and spatial resolution of 26.7 lp mm^{-1}. This enables real-time polarization-modulated X-ray imaging *via* enantioselective CPRL detection. Additionally, X-ray penetration facilitates enantioselective decryption of subsurface polarization patterns, offering potential for anticounterfeiting technology and medical diagnosis with intrinsic security.

Received 20th March 2026
Accepted 11th May 2026

DOI: 10.1039/d6sc02304e

rsc.li/chemical-science

Introduction

X-ray imaging is vital for clinical diagnostics and industrial inspection because of its superior ability to penetrate materials. In these systems, scintillators play a key role by converting high-energy X-ray photons into visible radioluminescence.[1,2] However, conventional scintillators emit only unpolarized light, restricting imaging to static, intensity-based methods.[3] The development of scintillators capable of generating circularly polarized radioluminescence (CPRL) offers potential for real-time, polarization-sensitive imaging.[4] This advancement could enhance both functional imaging capabilities and data security.[5]

Chirality-integrated materials, utilizing circularly polarized luminescence to encode multidimensional data, are emerging as key platforms for advanced optical applications in information security and storage.[6–8] Unlike conventional anticounterfeiting methods based on surface luminescence or reflectance under UV or visible light, X-ray-activated chiral scintillators offer a breakthrough through their deep-penetrating capability.[9,10] This allows covert data embedding and retrieval within complex nanostructures, which is critical for high-security applications.[11,12]

Despite these advantages, research on chiral scintillators remains nascent.[13] Recently, Li *et al.* synthesized chiral Pb(II)-based scintillators and demonstrated polarization-dependent radioluminescence, offering potential to reduce crosstalk in X-ray imaging.[14] Yao *et al.* developed chiral Mn(II)-based scintillators that achieved circularly polarized radioluminescence with a polarization degree of approximately 0.01.[15] However, these materials are restricted to bulk forms, hindering integration into pixelated arrays essential for X-ray imaging.[16] Moreover, the degree of circular polarization (P value) in radioluminescence, ranging from 10^{-3} to 10^{-2}, remains significantly below the threshold required for practical CPRL-based applications.[17,18]

A bilayer architecture combining halide perovskite nanocrystals with a self-assembled chiral cholesteric liquid crystal (CLC) matrix offers a promising solution.[19–21] Recently, Gu *et al.* realized color-tunable single-mode chiral microlasers based on $CsPbBr_3$ microrods encapsulated in a CLC layer, achieving g_{lum} as high as 1.62.[22] Feng *et al.* fabricated circularly polarized perovskite photodetectors by integrating $MAPbBr_3$ single crystals with free-standing CLC polymer films, reaching a record photocurrent dissymmetry factor of 1.95.[23] Yuan *et al.* demonstrated a chirality-invertible circularly polarized amplified spontaneous emission source, enabling dynamic tuning of g_{lum} from −1.38 to +1.22.[24] The perovskite nanocrystals serve as nanoscintillators, featuring tunable radioluminescence wavelengths, narrow spectral linewidths, and compatibility with scalable patterning methods such as screen printing.[25,26] Meanwhile, the chiral CLCs form periodic helical structures when chiral dopants are introduced into nematic hosts.[27] CLCs possess a periodic helical structure that enables enantioselective Bragg reflection of incident light. Within the reflection band, right-handed CLCs strongly reflect right-handed

School of Chemistry and Chemical Engineering, Nanjing University of Science and Technology, Nanjing, 210094, China. E-mail: chenluhe@njust.edu.cn

† These authors contributed equally to this work.

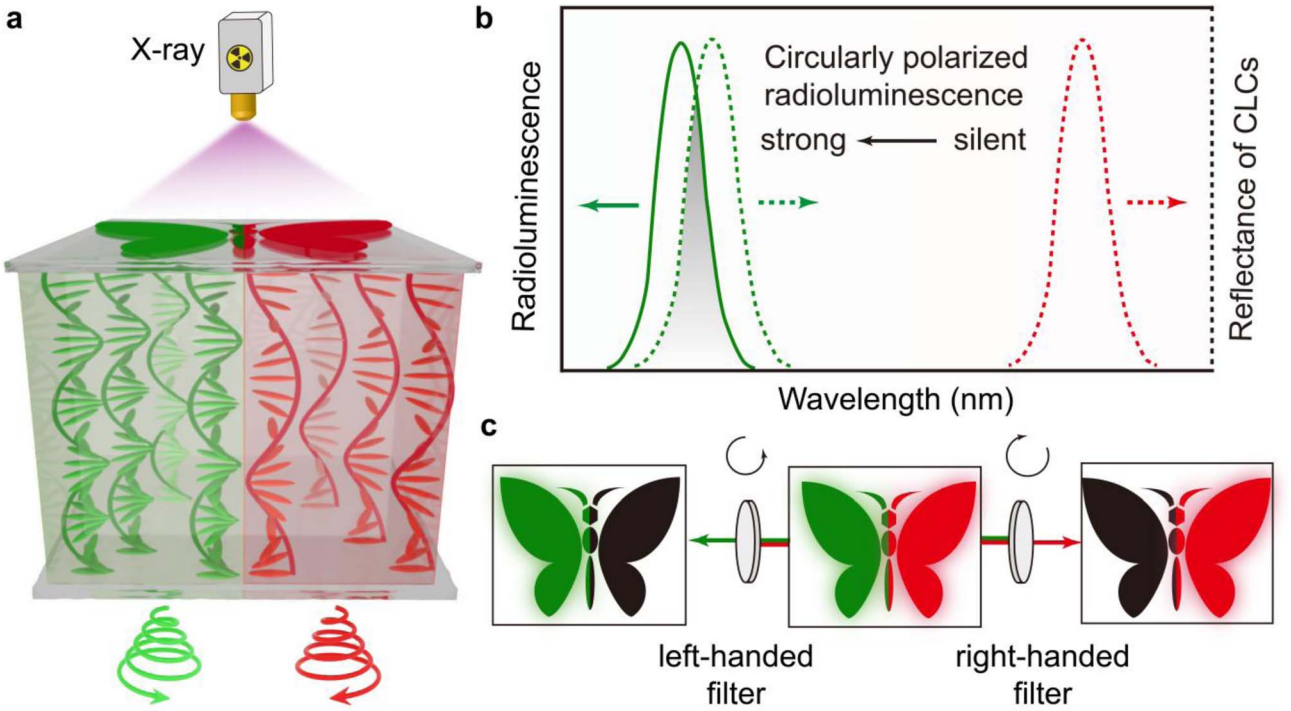

Fig. 1 Schematic of circular polarization radioluminescence generation from a patterned chiral nanoscintillator architecture. (a) In our design, the bilayer architecture consists of patterned perovskite nanocrystals ($FAPbClBr_2$, $FAPbBr_3$ or $FAPbBrI_2$ nanocrystals, top layer) that emit tunable unpolarized radioluminescence under X-ray irradiation, and cholesteric liquid crystals (CLCs, bottom layer) featuring periodic helical structures that convert the unpolarized radioluminescence to CPRL through enantioselective reflection and transmission optical processes. (b) The CPRL intensity strongly depends on spectral matching, where maximum circular polarization occurs when the CLC reflection band overlaps with the perovskite emission peak, while spectral mismatch leads to negligible circular polarization. (c) Under X-ray irradiation, a "butterfly" pattern demonstrates spatially controlled CPRL, where the left wing composed of $FAPbBr_3$-based *R*-architecture emits preferential *L*-CPRL (green emission) and the right wing formed by $FAPbBrI_2$-based *S*-architecture emits *R*-CPRL (red emission). Enantioselective decryption using a left-handed filter transmits only the *L*-CPRL green emission from the left wing while blocking *R*-CPRL (right wing dark), whereas a right-handed filter transmits the *R*-CPRL red emission from the right wing while blocking *L*-CPRL (left wing dark).

circularly polarized light while transmitting left-handed circularly polarized light, and *vice versa* for left-handed CLCs.[28,29] This property allows CLCs to function as circular polarization filters. When the emission spectrum of a luminescent material overlaps with the reflection band of CLCs, the transmitted component becomes highly circularly polarized.[30,31] Inspired by this effective filtering principle, this approach may break the entanglement in radioluminescence between circular polarization degree and intensity, enabling high-brightness and strongly chiral nanoscintillators for encrypted X-ray imaging.[32]

In this work, dynamic X-ray imaging is demonstrated using a compact bilayer architecture comprising patterned halide perovskite nanoscintillators and spectrum-matched CLCs, whose photonic bandgap aligns with the perovskite emission band (Fig. 1a and b). This design achieves a circular polarization degree of 0.75 in room-temperature radioluminescence, along with X-ray imaging performance featuring a detection limit of 204 nGy s^{-1} and spatial resolution of 26.7 lp mm^{-1}. Encrypted X-ray imaging is realized *via* polarization-selective detection without structural reconfiguration, allowing chiroptical encryption in subsurface environments beyond conventional limits (Fig. 1c).

Results and discussion

Colloidal $FAPbClBr_2$, $FAPbBr_3$ and $FAPbBrI_2$ nanocrystals were synthesized using the ligand-assisted reprecipitation technique.[33] Specifically, a DMF solution containing PbX_2 and FAX (X = Cl, Br, I) precursors, with oleic acid and oleylamine as ligands, was rapidly injected into vigorously stirred chloroform at room temperature, leading to the immediate formation of nanocrystals. The ionic nature of the reaction caused fast nucleation and growth kinetics, with nanocrystals forming within seconds.[34] The emission colors of perovskite nanocrystals were systematically tuned by controlling the halide composition ($I^-/Br^-/Cl^-$ ratio), which directly modulates the bandgap of nanocrystals (Fig. S1). This bandgap engineering was verified by the characteristic blue-shift in UV-Vis absorption spectra observed with increasing Br^-/Cl^- content (Fig. S2). This compositional variation was also confirmed by X-ray diffraction (XRD) analysis (Fig. S3). Notably, mixed-halide compositions exhibited distinct variations in XRD patterns. The diffraction peaks of $FAPbBrI_2$ shifted to higher angles compared to $FAPbBr_3$, whereas those of $FAPbBrI_2$ shifted to lower angles. Furthermore, transmission electron microscopy (TEM)

confirmed the crystal morphology of synthesized $FAPbBr_3$ nanocrystals, which formed monodisperse nanocubes with an average size of approximately 20 nm (Fig. 2a). The clearly perovskite lattice showed a characteristic spacing of 0.21 nm, corresponding to the (022) plane of the cubic nanostructure, demonstrating the excellent crystalline quality of the nanocrystals.[35,36] This nanoscale dimensionality facilitates high-resolution patterning applications.

Owing to the scintillation properties of perovskite nanocrystals, we incorporated them into polysulfone to fabricate ~200 μm-thick nanoscintillator films.[37] The radioluminescence intensity of prepared nanoscintillators exhibits a linear increase with rising X-ray dose, demonstrating dose-rate responsiveness. Specifically, the $FAPbBr_3$ nanoscintillators exhibited high X-ray sensitivity across varying dose rates, producing intense green radioluminescence at 575 nm (Fig. 2d). In comparison, $FAPbClBr_2$ and $FAPbBrI_2$ nanoscintillators generated cyan and red radioluminescence with peaks at 525 nm and 700 nm, respectively (Fig. S4). Meanwhile, the detection limit refers to the lowest measurable X-ray dose rate that can be distinguished from noise. Performance evaluation revealed the $FAPbBr_3$@polysulfone film achieved a low detection limit of 204 nGy s^{-1}. Comparatively, the $FAPbClBr_2$@polysulfone and $FAPbBrI_2$@polysulfone films exhibited detection limits of 262 nGy s^{-1} and 238 nGy s^{-1}, respectively (Fig. 2b). Critically, all three detection limit values are lower than the standard dose rate required for medical X-ray diagnostics (5.5 μGy s^{-1}), suggesting the potential of perovskite nanoscintillators for high-performance scintillation screens.[38,39] We further employed these nanoscintillator films to successfully image an electronic chip's internal structure and produce high-contrast radiographs, validating their practical utility (Fig. 2c). This high-resolution capability marks an advancement in X-ray imaging technology.

Quantitative assessment of image quality was performed through modulation transfer function (MTF) measurements using X-ray edge imaging and the slanted-edge method. The $FAPbBr_3$@polysulfone film achieved a spatial resolution of 26.7 lp mm^{-1} at MTF = 0.2 (Fig. 2e), outperforming both $FAPbClBr_2$@polysulfone and $FAPbBrI_2$@polysulfone films (Fig. S5). This resolution capability was independently validated by line-pair card imaging, which clearly resolved features at 20

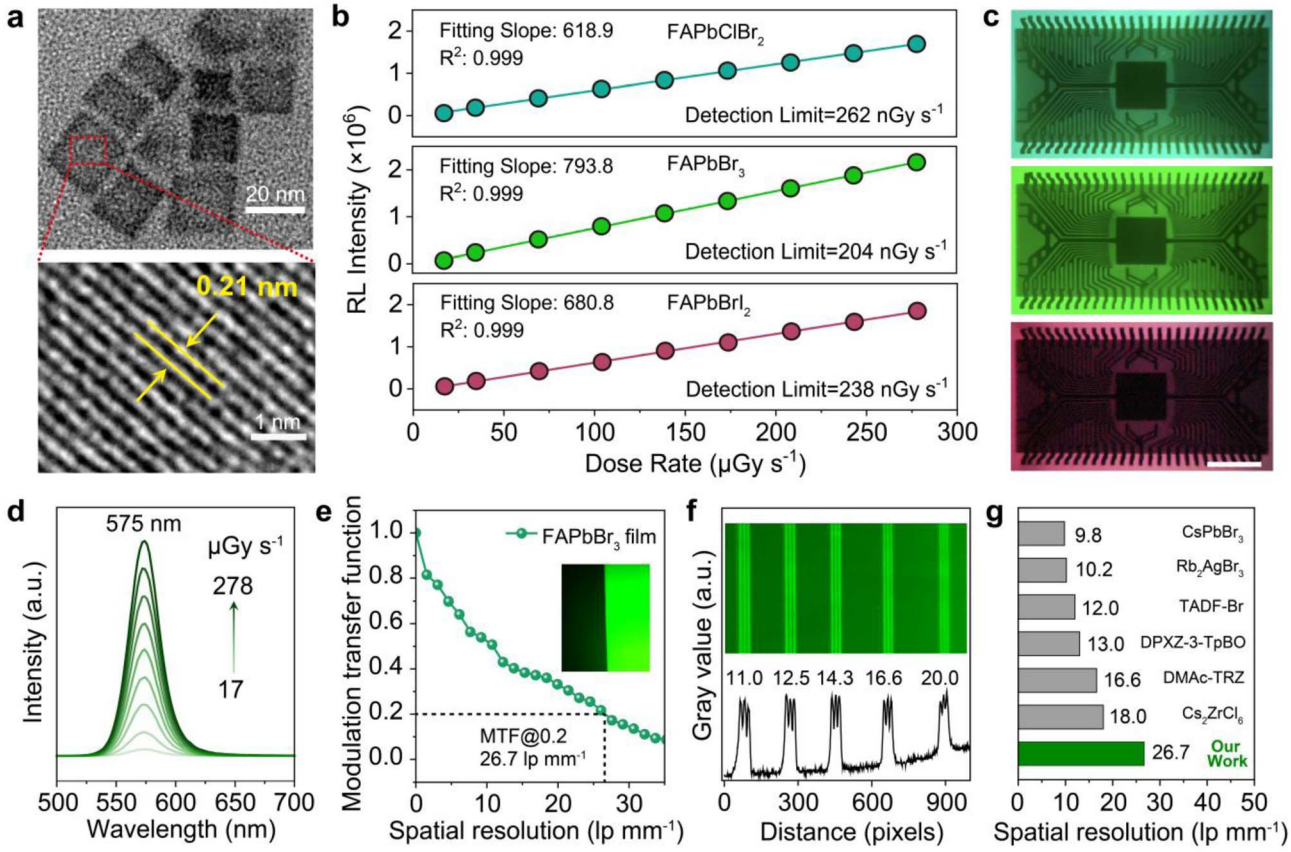

Fig. 2 X-ray imaging performance of nanoscintillators. (a) TEM and high-resolution transmission electron microscopy (HRTEM) of $FAPbBr_3$ nanocrystals. (b) X-ray detection limit of $FAPbClBr_2$, $FAPbBr_3$ and $FAPbBrI_2$ nanocrystals embedded in the polysulfone film. (c) High-resolution X-ray imaging of a chip through $FAPbClBr_2$, $FAPbBr_3$ and $FAPbBrI_2$ nanocrystals embedded in the polysulfone film with a thickness of ~200 μm. Scale bar: 5 mm. (d) Radioluminescence spectra of the $FAPbBr_3$@polysulfone film under different X-ray dose rates. (e) Modulation transfer function (MTF) of X-ray imaging (inset) obtained from the $FAPbBr_3$@polysulfone film. (f) X-ray imaging of a standard line-pair card ranging from 11 to 20 lp mm^{-1}. (g) Comparison of spatial resolution among $FAPbBr_3$ nanoscintillators and representative organic and inorganic scintillators.

lp mm^{-1} (Fig. 2f and S6). Importantly, the spatial resolution exceeds values reported for most organic and inorganic scintillators, indicating superior performance for high-resolution X-ray imaging applications (Fig. 2g).[40–45]

To generate CPRL under X-ray irradiation, we engineered a bilayer architecture combining patterned perovskite nanoscintillators with self-assembled cholesteric liquid crystals (CLCs) through enantioselective reflection and transmission optical processes (Fig. 3a). The CLC cells were fabricated by filling the nematic liquid crystal SLC1717 doped with chiral *R*/*S*-5011 between two quartz plates. Through precise control of the mass ratio between *R*/*S*-5011 and SLC1717, we achieved widely tunable circular dichroism (CD) signals across the visible spectrum, with all configurations exhibiting strong CD intensities of ~1580 mdeg (Fig. 3b, g and S7).[46] These CD signals, coupled with the characteristic oily streak texture observed under polarized optical microscopy (POM), collectively confirm the successful formation of a well-aligned cholesteric phase

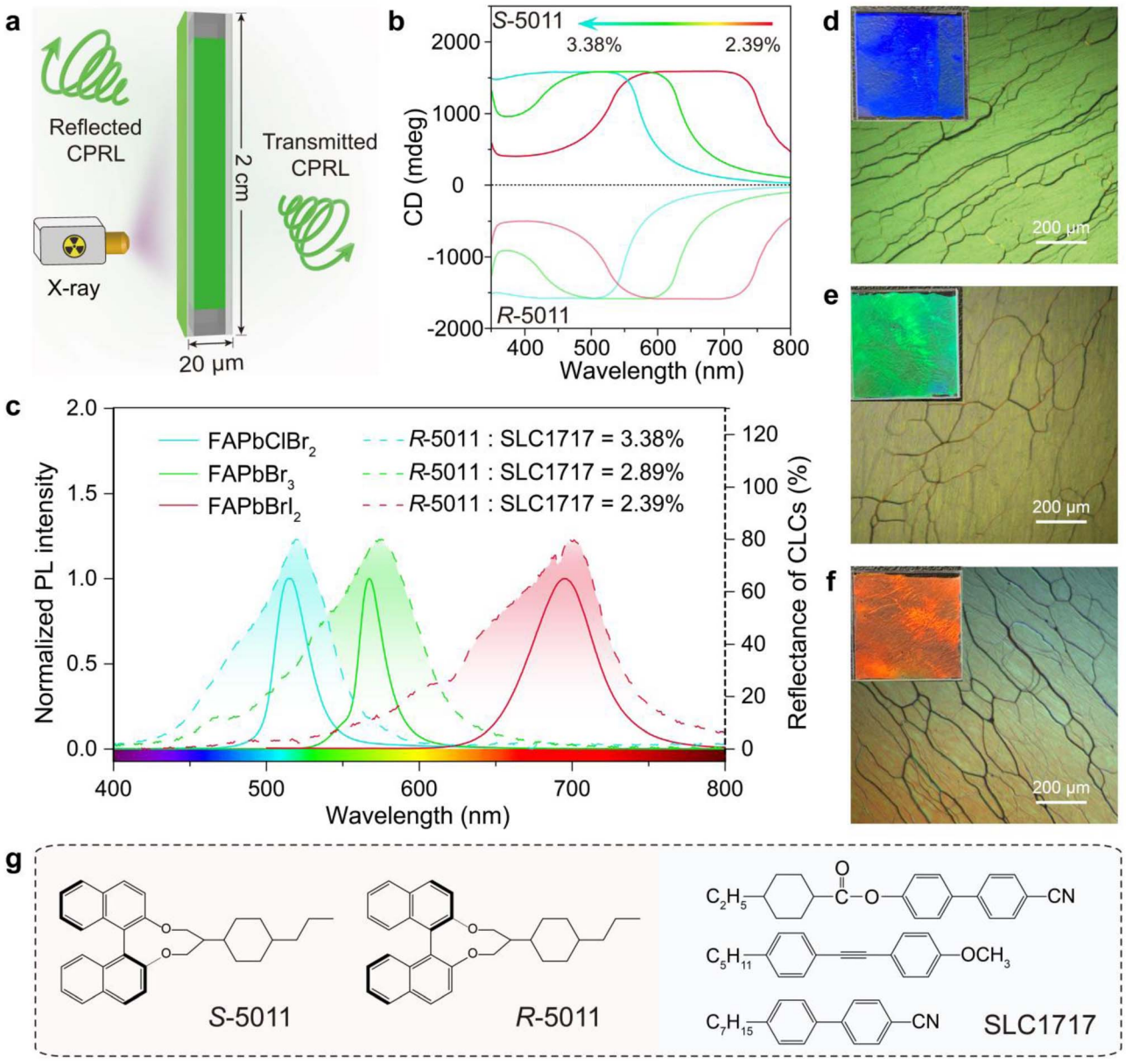

Fig. 3 Optical characterization of the perovskite-CLCs bilayer architecture. (a) Schematic illustration of CPRL generation from the chiral nanoscintillator architecture. The designed architecture consists of a 20 μm-thick CLCs layer in a liquid crystal cell (4 cm^2 active area), with surface-coated perovskite nanoscintillators. Upon X-ray irradiation, these perovskite nanoscintillators emit unpolarized radioluminescence that is converted to CPRL by CLCs. (b) CD spectra of chiral architectures comprising *S*/*R*5011 and SLC1717 at varying weight ratios (from 2.39% to 3.38%). (c) Reflection spectra of SLC1717 with 3.38%, 2.89% and 2.39% *S*-5011 (dashed line) and the photoluminescence spectra ($\lambda_{ex} = 365$ nm) of $FAPbClBr_2$, $FAPbBr_3$, and $FAPbBrI_2$ perovskite nanocrystals (solid line). (d–f), Top-view POM images of CLCs, with *S*-5011/SLC1717 weight ratios of (d) 3.38%, (e) 2.89% and (f) 2.39%. Insets show their top-view photographs under white light. (g) Molecular structure of chiral dopants (*S*-5011 and *R*-5011) and nematic host SLC1717.

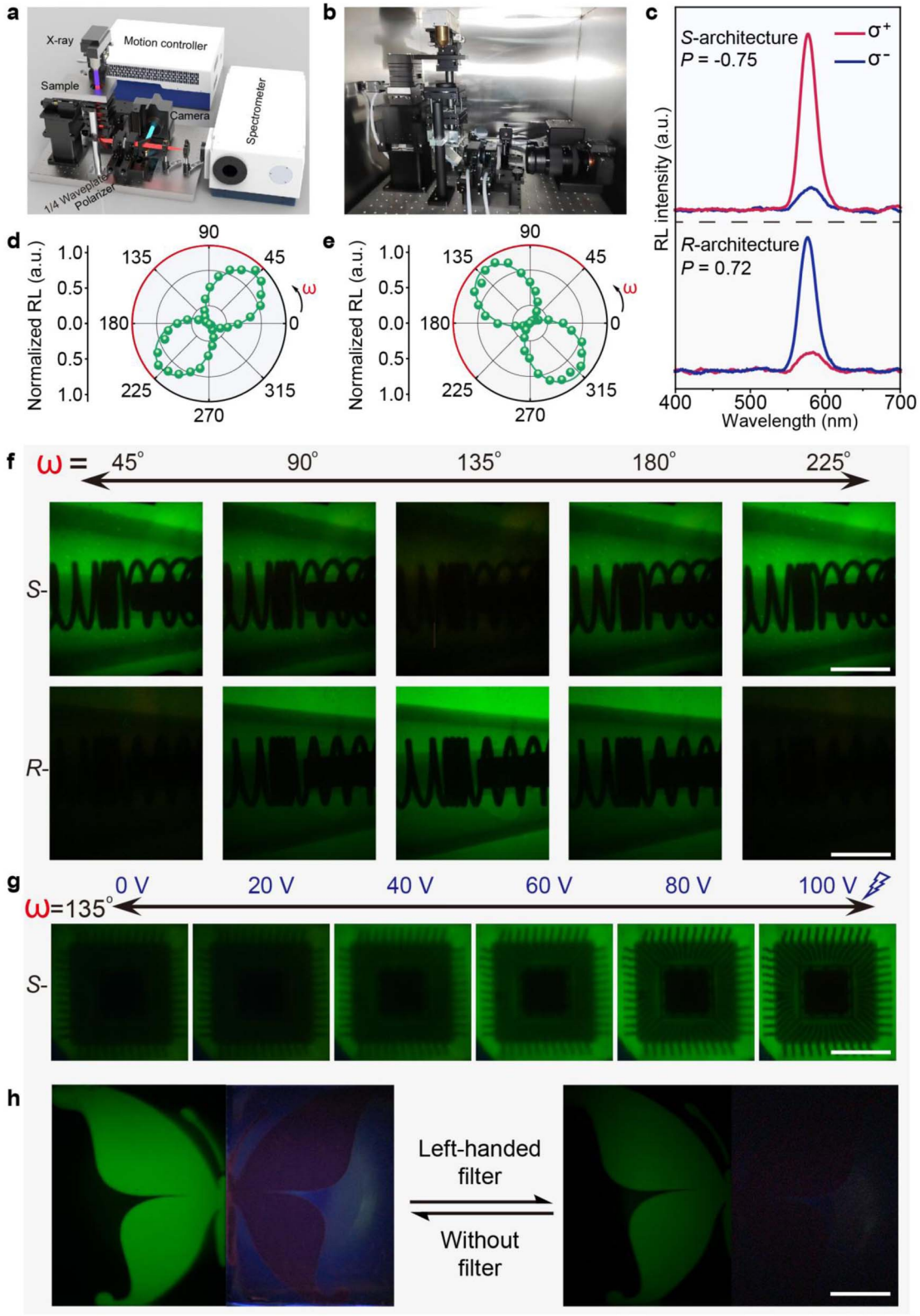

Fig. 4 Dynamic X-ray imaging using chiral nanoscintillator architectures. (a) Schematic illustration and (b) overall photograph of the optical setups for polarization-resolved radioluminescence spectroscopy and X-ray imaging, which are safely placed in a lead box. The primary optical components consist of a 1/4 waveplate and a linear polarizer. Upon X-ray excitation, chiral nanoscintillator architectures generate CPRL, which passes sequentially through the 1/4 waveplate and linear polarizer before detection by a spectrometer or camera. (c) Polarization-resolved radioluminescence spectra of $FAPbBr_3$-based *S*- and *R*-architectures under X-ray excitation. The σ^- and σ^+ represent the intensities of left-handed and right-handed CPRL, respectively. Emission intensity of (d) *R*-CPRL and (e) *L*-CPRL as a function of polarization angles with the 1/4 waveplate in the polar coordinate system, where the polar angle ω stands for the transmission angle of the polarizer. (f) Polarization-encoded

(Fig. 3d–f). It is important to clarify that the strong CD signals originate primarily from the enantioselective Bragg reflection of the helical structure rather than from the intrinsic circular dichroism of the chiral dopants themselves (Fig. S8). This periodic helical arrangement results in significant reflection within specific wavelength ranges, which manifests as apparent absorption peaks in CD spectroscopy measurements. Both the reflected and transmitted light within this characteristic wavelength band exhibit circular polarization. The *P* value reaches its maximum when the incident radioluminescence wavelength aligns with the peak of the CLC reflection spectrum. Therefore, obtaining a liquid crystal whose reflection spectrum covers the radioluminescence range of the perovskite nanoscintillator is essential for efficient CPRL generation.

The reflection spectra of the CLCs were measured using an integrating system with combined xenon and tungsten lamp sources (Fig. S9).[47] Targeting the emission wavelengths of $FAPbBrI_2$, $FAPbBr_3$, and $FAPbClBr_2$ excited by X-rays, by systematically adjusting the chiral *R*/*S*-5011 doping concentration, we tuned the helical pitch *p* of the CLCs, thereby shifting the Bragg reflection wavelength according to the relationship:[48]

$$\lambda_B = \bar{n}p$$

where $\bar{n}$ is the average refractive index and λ_B is the Bragg reflection wavelength. At specific doping ratios (2.39%, 2.89%, and 3.38%), we achieved the reflectance spectra of CLCs to cover the emission peaks of $FAPbClBr_2$ (525 nm), $FAPbBr_3$ (575 nm), and $FAPbBrI_2$ (700 nm) (Fig. 3c). Meanwhile, these reflection spectra correspond to the red, green, and blue structural colors exhibited by the three different doping ratios of liquid crystals when viewed perpendicular to the liquid crystal cell under natural light (insets in Fig. 3d–f). Under the condition of spectral matching, the quartz plate filled with liquid crystals was coated with a chloroform solution containing polysulfone and perovskite, resulting in a composite structure consisting of the perovskite@polysulfone film, a quartz plate, a liquid crystal layer, and another quartz plate, as confirmed by cross-sectional scanning electron microscopy (Fig. S10).

We next investigated the characteristics of CPRL in the chiral nanoscintillator architecture at room temperature using polarization-resolved radioluminescence spectroscopy under X-ray excitation (Fig. 4a and b).[49,50] The circular polarization degree (*P*) in X-ray radioluminescence, a key parameter for quantifying the CPRL, is calculated using the following equation:w

$$P = \frac{\sigma^- - \sigma^+}{\sigma^- + \sigma^+}$$

here *P* ranges from −1 to 1, and σ^- and σ^+ represent the intensities of left-handed and right-handed CPRL, respectively.[51] Notably, the *S*-architecture (*S*-CLCs with $FAPbBr_3$ nanoscintillators) generated right-handed CPRL (*R*-CPRL) with a maximum *P* value of −0.75 at 575 nm, while the *R*-architecture (*R*-CLCs with $FAPbBr_3$) yielded left-handed CPRL (*L*-CPRL) with a maximum *P* value of 0.72, approximately 70 times higher than previous reports (Fig. 4c).[15] In the selection of the liquid crystal host, SLC-1717 was chosen for its high clearing point (92 °C), which ensures a stable cholesteric phase under ambient conditions. For the chiral dopant, *R*/*S*-5011 was selected after comparative evaluation against alternatives such as *R*-811 and LC756, which yielded lower polarization degrees ($|P| \sim 0.5$ in Fig. S11). Thus, the combination of SLC-1717 and *R*/*S*-5011 represents the effective system for generating CPRL. This strong polarization contrast sharply differs from achiral $FAPbBr_3$ nanoscintillators alone, which exhibited a *P* value of 0, confirming the essential role of chiral CLCs (Fig. S12). To further validate the spectral matching mechanism, we performed control experiments using spectrally mismatched systems (*e.g.*, green-emitting $FAPbBr_3$ with red- or blue-reflecting CLCs). In these cases, the detected intensities for left- and right-handed CPRL were nearly identical, confirming the absence of CPRL (Fig. S13). This contrast underscores the necessity of precise spectrum matching for effective CPRL generation.

We next evaluated the stability of the bilayer architecture under continuous X-ray irradiation, temperature variation, and ambient exposure. When stored in air and measured hourly over 5 hours, the *P* value remained stable at approximately 0.7 (Fig. S14 and S15). Under continuous X-ray irradiation, however, the *P* value exhibited a temporary decline, attributed to molecular reorientation in the CLCs caused by heating from the X-ray source. The *P* value recovered to its initial level after the architecture was cooled (Fig. S16). Furthermore, temperature-dependent measurements showed that the *P* value decreased from 0.7 to 0.5 as the temperature increased from room temperature to 70 °C, and dropped abruptly to zero at the clearing point of the liquid crystal host (85 °C) (Fig. S17).

The CPRL from the chiral nanoscintillator architecture was further confirmed through complementary techniques. Transmittance measurements were performed by passing the radioluminescence through a 1/4 waveplate, which converts the CPRL into linearly polarized light, followed by a rotating linear polarizer.[52] As expected, right-handed and left-handed CPRL were transformed into linearly polarized light with orthogonal polarization planes (Fig. 4d and e). Additionally, UV-excited circularly polarized photoluminescence (CPPL) was measured using a JASCO CPL-300 spectrometer equipped with a monochromator-coupled Xe lamp excitation source. This result further verifies the capability of the liquid crystal matrix to induce a chiral environment under photoexcitation (Fig. S18). These findings confirm the successful generation of high-quality CPRL from the chiral architecture.

dynamic X-ray imaging of a ballpoint pen using the $FAPbBr_3$-based *S*-architecture, with polarization-state analysis performed by rotating the polarizer in the detection channel. Scale bar: 5 mm. (g) Dynamic X-ray imaging of a chip using the $FAPbBr_3$-based *S*-architecture under various external electric fields (the polar angle ω is 135°). Scale bar: 5 mm. (h) Enantioselective decryption of a subsurface "butterfly" pattern using circular polarizing filters under X-ray irradiation. Scale bar: 5 mm.

To demonstrate the broad applicability of the design, we extended the investigation to $FAPbClBr_2$ and $FAPbBrI_2$ nanoscintillators, employing spectrum-matched CLCs. Both perovskite compositions successfully generated intense CPRL: the $FAPbClBr_2$-based architecture emitted at 525 nm, while the $FAPbBrI_2$-based architecture emitted at 700 nm. More importantly, both architectures achieved $|P|$ values exceeding 0.5 (Fig. S19). This consistent generation of intense CPRL across various chiral nanoscintillator architectures, operating at distinct wavelengths, powerfully underscores the inherent universality of the chiral bilayer design.

With chiral nanoscintillator architectures in hand, we next explored dynamic encrypted X-ray imaging *via* rotating the polarizer in the detection channel (Fig. 4f). First, the imaging capability of the *S*-architecture has been verified. Performance evaluation revealed that the *S*-architecture achieved a low detection limit of 244 nGy s^{-1}, which is still at a relatively excellent level (Fig. S20). In terms of resolution, The *S*-architecture achieved a spatial resolution of 29.8 lp mm^{-1} at MTF = 0.2 (Fig. S21). The resolution capability was independently validated by line-pair card imaging, which clearly resolved features at 20 lp mm^{-1} (Fig. S22). RL spectra of the *S*-architecture and $FAPbBr_3$@polysulfone film measured under the same conditions indicate the luminous intensity loss caused by the CLCs, which is approximately 47.83% (Fig. S23). And the *S*-architecture displays radioluminescence light yields as 5415 photons MeV^{-1} (Fig. S24). The $FAPbBr_3$-based *S*-architecture was used as a representative system, which generates intense *R*-CPRL. When rotating the polarizer to 45°, maximum *R*-CPRL transmission produced X-ray imaging with optimal sharpness and contrast, revealing internal details of a ballpoint pen. Progressive rotation to 90° substantially decreased *R*-CPRL transmission, resulting in degraded image resolution and obscured internal features. At 135° orientation, *R*-CPRL transmission minimized to near-zero levels while allowing only weak residual *L*-CPRL transmission, effectively concealing the imaged ballpoint pen. Continued rotation to 225° (functionally equivalent to 45°) restored full imaging performance, completing the modulation cycle. The emission from the *R*-architecture and that from the *S*-architecture exhibit complementary intensity variations upon rotating the polarizer. Specifically, when the polarizer is oriented to suppress the emission from the *S*-architecture, the *R*-architecture signal becomes enhanced. Conversely, at polarizer angles that maximize the *S*-architecture signal, the *R*-architecture emission is significantly suppressed. This result further validates the polarization-dependent characteristics of designed architectures. This dynamic X-ray imaging results from polarization-selective detection of CPRL, enabling real-time adjustments without structural reconfiguration. Crucially, conventional achiral scintillators cannot achieve dynamic control as they emit unpolarized radioluminescence, producing only static X-ray images. Moreover, we demonstrated real-time electrical switching of the CPRL by applying an external electric field to the chiral nanoscintillator architectures. The electric field induced reorientation of liquid crystal molecules, which altered the helical structure of the CLCs and enabled *in situ* tuning of the $|P|$ values (Fig. S25). As a result, X-ray imaging exhibited a reversible and dynamically tunable response under various electric fields (Fig. 4g). This electrically driven modulation showcases the unique capability of chiral nanoscintillator architectures and underscores their potential for programmable chiroptical devices.

Furthermore, the CPRL-active architecture integrates the deep-penetration capability of X-rays with nanoscintillator patterning to enable subsurface decryption of encrypted information.[53] As illustrated by a "butterfly" pattern displaying green and red wings under X-ray irradiation, encrypted information was enantioselectively revealed using circular polarizing filters (Fig. 4h). Specifically, the $FAPbBr_3$-based *R*-architecture emitted *L*-CPRL, producing a green emission pattern when imaged through a left-handed filter before the camera. Conversely, the $FAPbBrI_2$-based *S*-architecture emitted *R*-CPRL, which was blocked under identical filtering conditions. The suppressed red emission pattern immediately recovered upon filter removal, demonstrating on-demand reversible switching of the optical output. This real-time polarization-controlled switching enabled dynamic chiroptical encryption in subsurface environments beyond conventional access limits by taking advantage of the deep penetration of X-rays.

In summary, we develop a patterned chiral nanoscintillator architecture that achieves CPRL with a record polarization degree of 0.75, facilitating real-time polarization modulation for dynamic encrypted X-ray imaging. By integrating perovskite nanoscintillators with spectrum-matched CLCs, this design overcomes the intrinsic trade-off between the polarization degree and radioluminescence intensity. By exploiting the exceptional penetration depth of X-rays, this platform allows enantioselective decryption of polarization-encoded patterns beneath the surface, demonstrating potential for high-security anticounterfeiting and biomedical diagnostic applications.

Author contributions

Z. Y., Z. L. and K. W. conceived and designed the project. Z. L. analysed the data. C. H. wrote the manuscript. All authors participated in the discussion and analysis of the manuscript.

Conflicts of interest

The authors declare no competing interests.

Data availability

All relevant data that support the findings of this work are available from the corresponding author upon reasonable request.

Supplementary information (SI) is available. See DOI: https://doi.org/10.1039/d6sc02304e.

Acknowledgements

This work was supported by the fundamental research funds for the central universities, the National Natural Science

Foundation of China (52403008) and the Natural-Science-Foundation of Jiangsu Province (BK20241499).

References

1 X. Du, S. Zhao, L. Wang, H. Wu, F. Ye, K. H. Xue, S. Peng, J. Xia, Z. Sang, D. Zhang, Z. Xiong, Z. Zheng, L. Xu, G. Niu and J. Tang, *Nat. Photonics*, 2024, **18**, 162.
2 B. Hou, Q. Chen, L. Yi, P. Sellin, H.-T. Sun, L. J. Wong and X. Liu, *Nat. Rev. Electr. Eng.*, 2024, **1**, 639.
3 N. Gan, X. Zou, M. Dong, Y. Wang, X. Wang, A. Lv, Z. Song, Y. Zhang, W. Gong, Z. Zhao, Z. Wang, Z. Zhou, H. Ma, X. Liu, Q. Chen, H. Shi, H. Yang, L. Gu, Z. An and W. Huang, *Nat. Commun.*, 2022, **13**, 3995.
4 C. Wang, D. Liu, G. Wei, J. Huang, Z. An, X. Xu and B. Zhou, *Nano Lett.*, 2024, **24**, 9691.
5 Z. Yang, P. Zhang, X. Chen, Z. Hong, J. Gong, X. Ou, Q. Wu, W. Li, X. Wang, L. Xie, Z. Zhang, Z. Yu, X. Qin, J. Tang, H. Zhang, Q. Chen, S. Han and H. Yang, *Adv. Mater.*, 2023, **35**, 2309413.
6 Y. Sang, J. Han, T. Zhao, P. Duan and M. Liu, *Adv. Mater.*, 2020, **32**, 1900110.
7 Y. Zhang, S. Yu, B. Han, Y. Zhou, X. Zhang, X. Gao and Z. Tang, *Matter*, 2022, **5**, 837.
8 J. Liu, X. Zhou, X. Tang, Y. Tang, J. Wu, Z. Song, H. Jiang, Y. Ma, B. Li, Y. Lu and Q. Li, *Adv. Funct. Mater.*, 2025, **35**, 2414086.
9 H. Zhang, B. Zhang, C. Cai, K. Zhang, Y. Wang, Y. Wang, Y. Yang, Y. Wu, X. Ba and R. Hoogenboom, *Nat. Commun.*, 2024, **15**, 2055.
10 Z. Feng, J. Li, P. Yang, X. Xu, D. Wang, J. Li, C. Zhang, J. Li, H. Zhang, G. Zou and X. Chen, *Nat. Commun.*, 2025, **16**, 2264.
11 C. He, J. Qiu, Z. Mu, J. Chen, Y. Wu, Z. Jiang, P. Zhang, X. Qin, G. Xing and X. Liu, *Matter*, 2024, **7**, 475.
12 H. Zhang, B. Tang, B. Zhang, K. Huang, S. Li, Y. Zhang, H. Zhang, L. Bai, Y. Wu, Y. Cheng, Y. Yang and G. Han, *Nat. Commun.*, 2024, **15**, 3247.
13 H. Lee, C. U. Lee, J. Yun, C. S. Jeong, W. Jeong, J. Son, Y. S. Park, S. Moon, S. Lee, J. H. Kim and J. Moon, *Nat. Commun.*, 2024, **15**, 4672.
14 M. Li, Y. Wang, L. Yang, Z. Chai, Y. Wang and S. Wang, *Angew. Chem., Int. Ed.*, 2022, **61**, e202208440.
15 J. Yao, Q. Ding, H. Zeng, J. Wang, C. Shi, L. Xu and Z. Chen, *Angew. Chem., Int. Ed.*, 2025, **64**, e202502099.
16 M. Wang, X. Wang, B. Zhang, F. Li, H. Meng, S. Liu and Q. Zhao, *J. Mater. Chem. C*, 2023, **11**, 3206.
17 J. Lu, R. X. Qian, S. F. Lu, S. H. Wang, F. K. Zheng and G. C. Guo, *Adv. Funct. Mater.*, 2024, **34**, 2410219.
18 S. Li, X. Xu, L. Xu, H. Lin, H. Kuang and C. Xu, *Nat. Commun.*, 2024, **15**, 3506.
19 Q. Guo, M. Zhang, Z. Tong, S. Zhao, Y. Zhou, Y. Wang, S. Jin, J. Zhang, H.-B. Yao, M. Zhu and T. Zhuang, *J. Am. Chem. Soc.*, 2023, **145**, 4246.
20 S. Liu, X. Liu, Y. Wu, D. Zhang, Y. Wu, H. Tian, Z. Zheng and W. H. Zhu, *Matter*, 2022, **5**, 2319.
21 Y. Zhang, R. Liu and J. Chen, *Responsive Mater.*, 2025, **3**, e20250010.
22 H. Gu, H. Xu, C. Yang, Y. Feng, G. Gao, R. L. Z. Hoye, X. Hu, L. Polavarapu, G. Zhou and X.-F. Jiang, *Nano Lett.*, 2024, **24**, 13333–13340.
23 Y. Feng, G. Gao, X. Wen, Z. Chen, J. Huang, C. Yang, X.-F. Jiang, L. Polavarapu, G. Zhou and X. Hu, *Adv. Funct. Mater.*, 2025, **35**, 2421338.
24 M. Yuan, H. Xu, J. Liu, W. Zhou, M. Zhao, X.-F. Jiang, J. Chen, L. Polavarapu, G. Zhou and X. Hu, *ACS Energy Lett.*, 2025, **10**, 5684–5693.
25 Q. Chen, J. Wu, X. Ou, B. Huang, J. Almutlaq, A. A. Zhumekenov, X. Guan, S. Han, L. Liang, Z. Yi, J. Li, X. Xie, Y. Wang, Y. Li, D. Fan, D. B. L. Teh, A. H. All, O. F. Mohammed, O. M. Bakr, T. Wu, M. Bettinelli, H. Yang, W. Huang and X. Liu, *Nature*, 2018, **561**, 88.
26 Y. Wu, S. Wang, Z. Lin, L. Kang, J. Wu, Q. Chen and Z. Lin, *Angew. Chem.*, 2025, **137**, e202416062.
27 K. Yao, Z. Wang, F. Lin, S. Wang, H. Huang, W. Geng, J. Liu, F. Li, Y. Li, Z. Yuan, L. Hu and Z. Geng, *Adv. Funct. Mater.*, 2025, e00112.
28 Y. He, S. Lin, J. Guo and Q. Li, *Aggregate*, 2021, **2**, e141.
29 K. Horie, Y. Fujita, K. Kaneko, T. Hanasaki and K. Akagi, *ACS Appl. Mater. Interfaces*, 2025, **17**, 15988.
30 S. Li, Y. Tang, Q. Fan, Z. Li, X. Zhang, J. Wang, J. Guo and Q. Li, *Light: Sci. Appl.*, 2024, **13**, 140.
31 Y. Li, K. Yao, Y. Chen, Y. Quan and Y. Cheng, *Adv. Opt. Mater.*, 2021, **9**, 2100961.
32 Z. Liu, X. Liu, H. Zhang, L. Zeng, L. Niu, P. Chen, W. Fang, X. Peng, G. Cui and Q. Yang, *Angew. Chem., Int. Ed.*, 2024, **63**, e202407135.
33 D. Shi, V. Adinolfi, R. Comin, M. Yuan, E. Alarousu, A. Buin, Y. Chen, S. Hoogland, A. Rothenberger, K. Katsiev, Y. Losovyj, X. Zhang, P. A. Dowben, O. F. Mohammed, E. H. Sargent and O. M. Bakr, *Science*, 2015, **347**, 519.
34 I. Levchuk, A. Osvet, X. Tang, M. Brandl, J. D. Perea, F. Hoegl, G. J. Matt, R. Hock, M. Batentschuk and C. J. Brabec, *Nano Lett.*, 2017, **17**, 2765.
35 W. Xu, R. Ji, P. Liu, L. Cheng, L. Zhu, J. Zhang, H. Chen, Y. Tong, C. Zhang, Z. Kuang, H. Zhang, J. Lai, K. Wen, P. Yang, N. Wang, W. Huang and J. Wang, *J. Phys. Chem. Lett.*, 2020, **11**, 10348.
36 H. Wang, W. Xu, Q. Wei, S. Peng, Y. Shang, X. Jiang, D. Yu, K. Wang, R. Pu, C. Zhao, Z. Zang, H. Li, Y. Zhang, T. Pan, Z. Peng, X. Shen, S. Ling, W. Liu, F. Gao and Z. Ning, *Light:Sci. Appl.*, 2023, **12**, 62.
37 Z. Li, C. Zhang, Y. Li, Y. Wu, W. Zhang and C. He, *J. Mater. Chem. C*, 2025, **13**, 1181.
38 J. Xu, R. Luo, Z. Luo, J. Xu, Z. Mu, H. Bian, S. Y. Chan, B. Y. H. Tan, D. Chi, Z. An, G. Xing, X. Qin, C. Gong, Y. Wu and X. Liu, *Nat. Photonics*, 2025, **19**, 71.
39 J. Wang, O. Shekhah, O. M. Bakr, M. Eddaoudi and O. F. Mohammed, *Chem*, 2025, **11**, 102273.
40 J. H. Heo, D. H. Shin, J. K. Park, D. H. Kim, S. J. Lee and S. H. Im, *Adv. Mater.*, 2018, **30**, 1801743.
41 M. Zhang, X. Wang, B. Yang, J. Zhu, G. Niu, H. Wu, L. Yin, X. Du, M. Niu, Y. Ge, Q. Xie, Y. Yan and J. Tang, *Adv. Funct. Mater.*, 2021, **31**, 2007921.

42 J. Wang, L. Gutiérrez -Arzaluz, X. Wang, T. He, Y. Zhang, M. Eddaoudi, O. M. Bakr and O. F. Mohammed, *Nat. Photonics*, 2022, **16**, 869.
43 W. Yang, C. Xie, T. Chen, X. Yin, Q. Lin, S. Gong, Z. Quan and C. Yang, *Angew. Chem., Int. Ed.*, 2024, **63**, e202402704.
44 W. Ma, Y. Su, Q. Zhang, C. Deng, L. Pasquali, W. Zhu, Y. Tian, P. Ran, Z. Chen, G. Yang, G. Liang, T. Liu, H. Zhu, P. Huang, H. Zhong, K. Wang, S. Peng, J. Xia, H. Liu, X. Liu and Y. M. Yang, *Nat. Mater.*, 2022, **21**, 210.
45 F. Zhang, Y. Zhou, Z. Chen, M. Wang, Z. Ma, X. Chen, M. Jia, D. Wu, J. Xiao, X. Li, Y. Zhang, Z. Shi and C. Shan, *Adv. Mater.*, 2022, **34**, 2204801.
46 C. He, Z. Feng, S. Shan, M. Wang, X. Chen and G. Zou, *Nat. Commun.*, 2020, **11**, 1188.
47 H. Hu, M. He, X. Liang, M. Li, C. Yuan, B. Liu, X. Liu, Z. G. Zheng and W. H. Zhu, *Matter*, 2023, **6**, 3927.
48 M. E. McConney, M. Rumi, N. P. Godman, U. N. Tohgha and T. J. Bunning, *Adv. Opt. Mater.*, 2019, **7**, 1900429.
49 G. Long, C. Jiang, R. Sabatini, Z. Yang, M. Wei, L. N. Quan, Q. Liang, A. Rasmita, M. Askerka, G. Walters, X. Gong, J. Xing, X. Wen, R. Quintero-Bermudez, H. Yuan, G. Xing, X. R. Wang, D. Song, O. Voznyy, M. Zhang, S. Hoogland, W. Gao, Q. Xiong and E. H. Sargent, *Nat. Photonics*, 2018, **12**, 528.
50 N. Yang, Z. Ling, W. Hou and C. He, *Adv. Funct. Mater.*, 2026, e31126.
51 G. Long, R. Sabatini, M. I. Saidaminov, G. Lakhwani, A. Rasmita, X. Liu, E. H. Sargent and W. Gao, *Nat. Rev. Mater.*, 2020, **5**, 423.
52 W. Lin, C. Yang, Y. Miao, S. Li, L. Zhang, X. F. Jiang, Y. Lv, B. Poudel, K. Wang, L. Polavarapu, C. Zhang, G. Zhou and X. Hu, *Adv. Mater.*, 2023, **35**, 2301573.
53 S. Li, H. Zhang, J. Zhong, B. Zhang, K. Zhang, Y. Zhang, L. Li, Y. Yang, Y. Wu and R. Hoogenboom, *J. Am. Chem. Soc.*, 2025, **147**, 20273.